Nanoscale

Accepted Manuscript

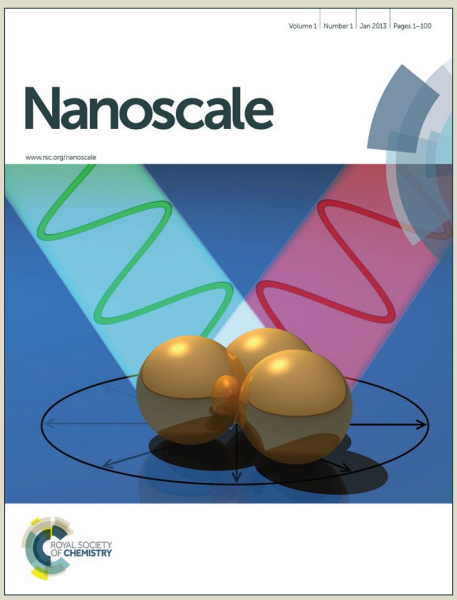

ROYAL SOCIETY OF CHEMISTRY

www.rsc.org/nanoscale

Nanostructured porous RuO_2/MnO_2 as highly efficient catalyst for high-rate Li–O_2 batteries

Guoqing Wang,[a] Liliang Huang,[a] Wei Huang,[a] Jian Xie,[*ab] Gaohui Du,[c] Shichao Zhang,[d] Peiyi Zhu,[e] Gaoshao Cao[b] and Xinbing Zhao[ab]

[a]*State Key Laboratory of Silicon Materials, School of Materials Science and Engineering, Zhejiang University, Hangzhou 310027, P. R. China. E-mail: xiejian1977@zju.edu.cn; Fax: +86-571-87951451; Tel: +86-571-87951451*
[b]*Key Laboratory of Advanced Materials and Applications for Batteries of Zhejiang Province, Hangzhou 310027, P. R. China*
[c]*Institute of Physical Chemistry, Zhejiang Normal University, Jinhua 321004, China*
[d]*Industrial Technology Research Institute of Zhejiang University, Hangzhou 310058, P. R. China*
[e]*School of Materials Science and Engineering, Beijing University of Aeronautics and Astronautics, Beijing 100191, P. R. China*

† Electronic supplementary information (ESI) available: SEM, XPS and XRD of the pristine electrodes, SAED and XPS of the discharge and charge electrodes, SEM images of the discharged electrodes with LiI, SEM images of the electrodes after recharge, voltage profiles of the Li–O_2 battery with graphene catalyst, voltage profiles of the Li–O_2 battery with RuO_2/G catalyst and the SEM image of the discharged electrodes, and voltage profiles of Li–MnO_2/G and Li–RuO_2/G batteries tested in pure Ar. See DOI:

Abstract

Despite recent advancements on Li–O_2 (or Li–air) batteries, great challenges still remain to realize the high-rate, long-term cycling. In this work, a binder-free, nanostructured RuO_2/MnO_2 catalytic cathode was designed to realize the operation of Li–O_2 batteries at high rates. At a current density as high as 3200 mA g^{-1} (or ~1.3 mA cm^{-2}), the RuO_2/MnO_2 catalyzed Li–O_2 batteries with LiI can sustain stable cycling of 170 and 800 times at limited capacities of 1000 and 500 mAh g^{-1}, respectively, with low charge cutoff potentials of ~4.0 and <3.8 V, respectively. The underlying mechanism of the high catalytic performance of MnO_2/RuO_2 was also clarified in this work. It was found that with the catalytic effect of RuO_2, Li_2O_2 can crystallize into a thin-sheet form and realize a conformal growth on sheet-like δ-MnO_2 at a current density up to 3200 mA g^{-1}, constructing a sheet-on-sheet structure. This crystallization behavior of Li_2O_2 not only defers the electrode passivation upon discharge but also renders easy decomposition of Li_2O_2 upon charge, leading to low polarizations and reduced side reactions. This work provides a unique design of catalytic cathodes capable of controlling Li_2O_2 growth and sheds light on the design of high-rate, long-life Li–O_2 batteries with potential applications in electric vehicles.

Introduction

One of the technical obstacles of current Li-ion batteries is the insufficient energy density, usually below 200 Wh kg^{-1},[1–3] although they have already been used as power sources for electric vehicles. In contrast, Li–O_2 (or Li–air) batteries can afford a much high energy density of 3505 Wh kg^{-1} via the reaction $2Li + O_2 \leftrightarrow Li_2O_2$.[3–6] Unfortunately, Li_2O_2 is electrically insulating,[7–10] and chemically/electrochemically reactive with organic electrolyte,[11–13] polymer binder[12–14] and conductive carbon.[15–18] In addition, the electrodes in Li–O_2 batteries should be specially designed with free space to accumulate Li_2O_2, fairly different from Li-ion batteries with a shuttle mechanism. The disadvantages of Li_2O_2 result in sluggish oxygen reduction/evolution reaction (ORR/OER) kinetics and thus poor battery performance. In recent years, great efforts have been made to improve the battery performance by optimizing electrode structures, developing stable electrolytes, using efficient catalysts, etc.[19–26]

Despite these efforts, great challenges still remain to develop practical Li–O_2 batteries with satisfactory rate capability and long cycle life at high rates, as generally required by electric vehicles. These obstacles are largely caused by the sluggish ORR/OER kinetics related to the insulating Li_2O_2. One of the effective strategies to enhance ORR/OER kinetics is to crystallize Li_2O_2 into favorable forms. First-principles calculations revealed that the surface of Li_2O_2 is half-metallic whereas the bulk Li_2O_2 is an insulator.[27] Theoretical study also indicated that thin Li_2O_2 deposits decompose at low potentials whereas thick Li_2O_2 deposits decompose at high potentials.[9] This suggests that the formation of low-dimensional Li_2O_2 is desirable to enhance the electrode kinetics. Experimental investigation found that the overall conductivity of Li_2O_2 could be increased by two orders of magnitude by decreasing its crystal size from micrometer to nanometer size.[10] The work by Hu et al. showed that the charge overpotentials of Li–O_2 batteries could be lowered by decreasing particle size of the pre-filled Li_2O_2.[28] Therefore, it is anticipated that the overpotentials (particularly charge overpotentials) could be decreased by crystallizing Li_2O_2 into low-dimensional forms during discharge. Recent work proven that noble metals on one-dimensional

carbon matrix are capable of directing thin-layered Li_2O_2 to grow conformally on the carbon matrices,[29–32] in contrast to the discs/toroids morphologies commonly observed on the carbon-based electrodes.[33,34]

Nevertheless, carbon materials are chemically unstable in contact with Li_2O_2 (or its intermediate LiO_2),[15–17] especially that with defects and functional groups.[18] Thus, the intimate contact of Li_2O_2 with carbon materials is unfavorable. In this regard, some metal oxides, such as MnO_2,[35–40] spinel-type oxides,[41–43] TiO_2,[44] and perovskite-type oxides,[45–47] are ideal supports for noble metals because of their good chemical/electrochemical stability towards Li_2O_2 (or LiO_2) and high catalytic activity for ORR/OER. Previous work showed that Au nanocrystals could direct the conformal growth of Li_2O_2 on the $NiCo_2O_4$ nanosheet.[48] Among various noble-metal-based catalysts, RuO_2 has received a special interest due to its superior catalytic performance for ORR/OER.[31,49–52] It was found that good catalytic performance can be achieved by loading RuO_2 on some stable oxides such as MnO_2 and TiO_2.[53–55] For example, Li−O_2 battery with RuO_2 catalyst could sustain a stable cycling of 130 times under 1770 mA g^{-1} at a limited capacity of 1000 mAh g^{-1},[54] by loading RuO_2 on a stable TiO_2/Ti support.[56]

However, compared with carbon materials, metal oxides usually show low electronic conductivity which limits the rate capability and high-rate cycling performance of Li–O_2 batteries. In this case, the architecture of the catalytic cathode is important to achieve high performance of Li–O_2 batteries. In this work, a unique design of catalytic cathode was proposed, where RuO_2-modified δ-MnO_2 nanosheets were directly deposited on graphene-coated nickel substrate by a facile hydrothermal route. It was found that RuO_2 is highly efficient in promoting the "wetting" of Li_2O_2 on MnO_2 nanosheets at high current rates. Namely, a conformal growth of Li_2O_2 sheets on MnO_2 sheets can be realized at high rates, which can alleviate and defer the electrode deactivation associated with low-conductive Li_2O_2 and MnO_2. The controlled growth of Li_2O_2 at high current rates is realized through the synergic effect of RuO_2 and MnO_2. RuO_2 is also highly efficient in catalytically decomposing Li_2O_2 at high current rates. The decomposition of Li_2O_2 can be further

promoted by using a soluble catalyst.

As a result, RuO_2/MnO_2-catalyzed Li–O_2 batteries with a soluble catalyst exhibit excellent rate capability and long cycle life at high rates. At a current density as high as 3200 mA g^{-1} (~1.3 mA cm^{-2}), the battery can demonstrate a low charge cutoff potential (3.84 V) and a high discharge cutoff potential (2.54 V). The battery can sustain a stable cycling up to 170 times at 3200 mA g^{-1} with a limited capacity of 1000 mAh g^{-1}. When the capacity is limited at 500 mAh g^{-1}, a stable cycling over 800 times can be achieved with a low charge cutoff potential (< 3.8 V). This work will shed light on the design of new catalysts enabling superior rate capability and high-rate cycling stability of Li–O_2 batteries with promising applications in electric vehicles.

Experimental section

Electrodes preparation and characterization

The detailed preparation procedure of δ-MnO_2 nanosheets on graphene-coated nickel foam (Ni/G) was described previously.[38] The loading of RuO_2 on MnO_2 nanosheets was performed by a facile solution impregnation approach. Briefly, the Ni/G supported MnO_2 was immersed in a $RuCl_3$ aqueous solution (0.16 mg mL^{-1}) with magnetic stirring for 3 h at room temperature. After rinsing with distilled water, the obtained product was heated at 300 °C for 2 h in Ar. The loadings of MnO_2 and RuO_2 are around 0.31 and 0.11 mg cm^{-2}, respectively. For comparison, RuO_2 was directly loaded on Ni/G by a similar route as on δ-MnO_2, where the pH of the $RuCl_3$ solution was adjusted to 5−6 by adding 0.2 M $NaHCO_3$ aqueous solution. The loading of RuO_2 on Ni/G is around 0.1 mg cm^{-2}. The phases present in the electrode were checked by X-ray diffraction (XRD) on a Rigaku D/Max-2550pc diffractometer using Cu K_α radiation (λ = 0.1541 nm). The chemical states of the electrode components were analyzed by X-ray photoelectron spectra (XPS) on a KRATOS AXIS ULTRA-DLD spectrometer using monochromatic Al K_α radiation ($h\nu$ = 1486.6 eV). The morphology and microstructure of the electrodes (or electrode components) were observed by scanning electron microscope (SEM) on a FEI-sirion microscope and transmission electron

microscopy (TEM) on a JEM 2100F microscope. The high-angle annular dark-field (HAADF)-scanning transmission electron microscopy (STEM) images and the energy dispersive X-ray spectrometry (EDX) mapping were carried out on a FEI Tecnai G^2 F20 microscope using an acceleration voltage of 200 kV.

Electrochemical measurements

Coin-type Li–O_2 batteries were assembled in an argon-filled glove box using metallic Li foil as anode, Ni/G supported RuO_2/MnO_2 (or MnO_2) as cathode (0.6 cm × 0.6 cm), and 1 M lithium-bis(trifluoromethanesulphonyl)imide (LiTFSI) in tetraethylene glycol dimethyl ether (TEGDME) as electrolyte. In some cases, 0.05 M LiI was added in the electrolyte. The electrodes were dried in a vacuum oven at 80 °C for 3 h before batteries assembly. The assembled coin batteries were purged with O_2 for 20 min and stayed at open voltage circuit (OCV) for 5 h before the electrochemical tests. Constant-current cycling was carried out using a Neware battery cycler (Shenzhen, China) in a voltage window of 2.0–4.5 V (vs. Li/Li^+). The specific capacity (mAh g^{-1}) and current density (mA g^{-1}) of the RuO_2/MnO_2-catalyzed batteries were normalized by the total mass of MnO_2 and RuO_2. For the MnO_2-catalyzed battery, the current density and specific capacity were normalized by the mass of MnO_2. The electrochemical tests were performed at 25 °C.

Results and discussion

MnO_2 was deposited directly on the skeleton of Ni/G, copying its three-dimensional (3D) interconnected scaffold structure, and the large pores in Ni foam are kept intact (ESI, Fig. S1a). This electrode design allows barrier-free diffusion of oxygen gas and Li ions, and excludes or minimizes the side reactions related to binder and carbon.[12–18] SEM indicates that the MnO_2 is assembled from nanosized sheets and exhibits a 3D porous structure (Fig. 1a and ESI, Fig. S1b). This 3D porous structure facilitates the diffusion of Li ions and deposition of the lithiation products.[57–59] As seen in Fig. 1b, the porous structure is preserved after RuO_2 decoration. High-magnification SEM in Fig. 1c shows that the surface of MnO_2 sheets is coated with

floccus-like substance, which is supported by TEM (ESI, Fig. S1d). The decoration of RuO_2 on MnO_2 sheets is more clearly seen in dark-field TEM and the corresponding EDS mapping (Fig. 1d–g). XPS confirms the formation of MnO_2 and RuO_2 (ESI, Fig. S2a−c). XRD patterns in Fig. S2d indicate that the MnO_2 is δ-MnO_2.

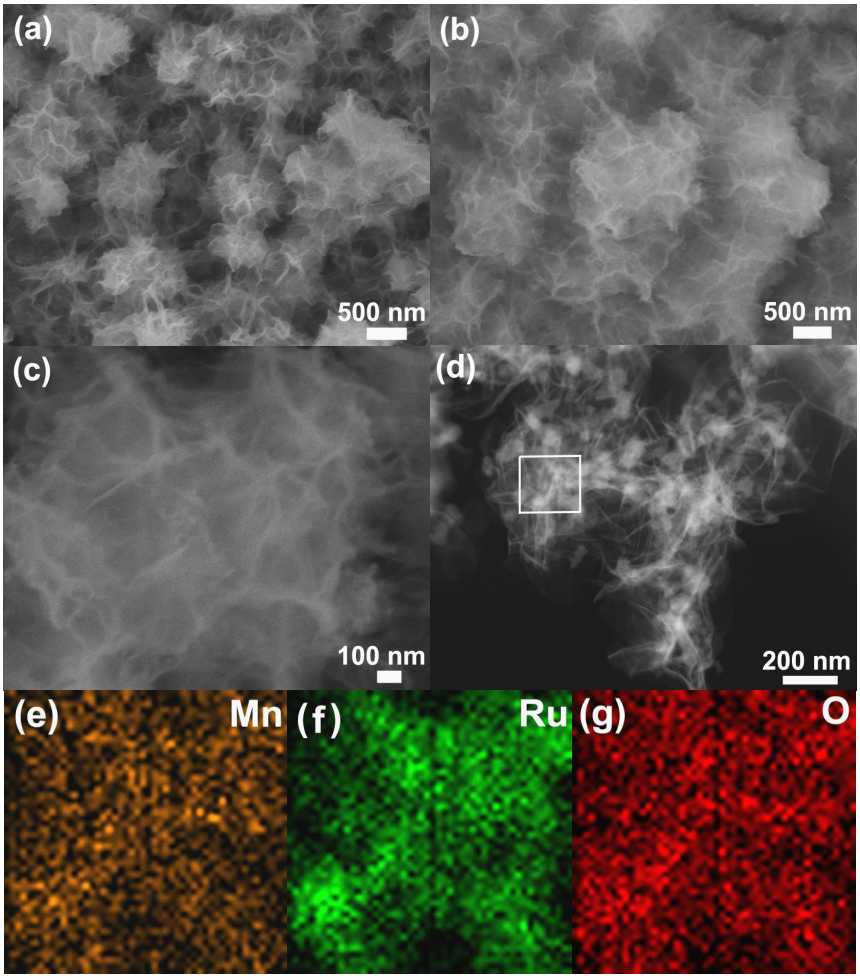

Fig. 1 (a) SEM image of MnO_2, (b,c) SEM images of RuO_2/MnO_2, (d) dark-field TEM image of RuO_2/MnO_2, and (e–f) EDS mapping of the marked domain in (d).

The catalytic activity of the catalysts for ORR and OER was evaluated by rate capability tests. Li–O_2 batteries with different catalysts were tested at various current densities (400–3200 mA g^{-1}) with the capacity limited at 1000 mAh g^{-1} as shown in Fig. 2. For comparison, the reversible potential (E_{rev} = 2.96 V) of nonaqueous Li–O_2 battery was also plotted. The current density and specific capacity were calculated normalized by the weight of MnO_2 or RuO_2+MnO_2 for the MnO_2

cathode and the RuO_2/MnO_2 cathode, respectively. Soluble catalysts such as LiI and MPT have shown the ability to catalytically oxidize Li_2O_2 with low overpotentials.[60,61] At a moderate current density of 400 mA g^{-1}, the batteries show similar discharge potentials and the discharge processes all occur at a high potentials (> 2.6 V) (Fig. 2a), indicating that the MnO_2 itself has a high catalytic effect for ORR at the moderate current density. In contrast, for the charge process, the batteries show a sharp difference depending on the catalysts used. The introduction of RuO_2 obviously lowers the charge overpotentials, which can be further lowered by adding LiI in the electrolyte. The charge cutoff potential can be reduced from 4.24 V for battery with MnO_2 catalyst to 3.60 V for battery with RuO_2/MnO_2 +LiI catalyst. As seen in Fig. 2b–d, at higher current rates, the Li–O_2 batteries with RuO_2 generally exhibit higher discharge potentials than those without RuO_2 especially at deep discharge states. This suggests that RuO_2 is highly efficient in catalyzing ORR at high current rates whereas bare MnO_2 is insufficient to support high-rate ORR. It seems that the addition of LiI shows minor influence on the ORR kinetics, and that RuO_2 and LiI show a similar ability to catalytically oxidize Li_2O_2. Note that Li–O_2 battery exhibits excellent rate capability with the joint catalytic effects of RuO_2, MnO_2 and LiI. Even at a current density as high as 3200 mA g^{-1} (~1.3 mA cm^{-2}), the battery could exhibit a low charge cutoff potential (3.84 V) and a high discharge cutoff potential (2.54 V). These results demonstrate that RuO_2/MnO_2 is a superior catalyst for high-rate ORR and OER.

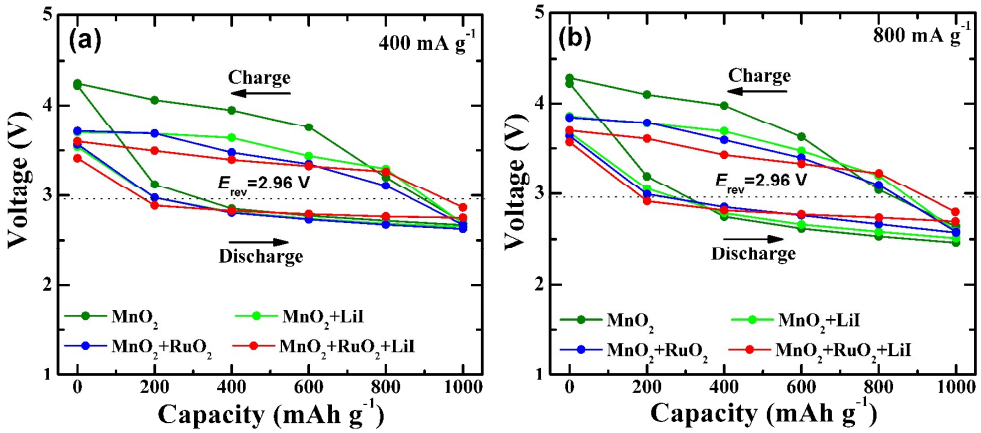

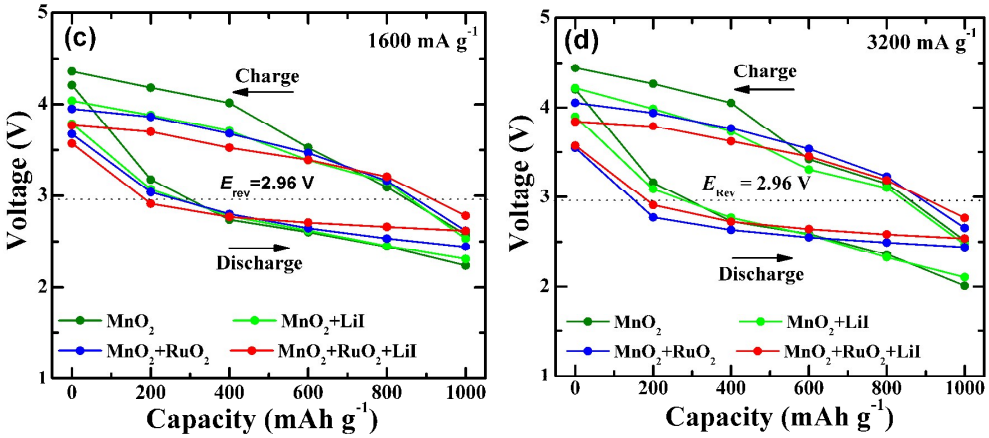

Fig. 2 Voltage as a function of capacity of the Li–O_2 batteries with different catalysts at current densities of (a) 400 mA g^{-1}, (b) 800 mA g^{-1}, (c) 1600 mA g^{-1}, and (d) 3200 mA g^{-1}.

SEM observations on the cycled electrodes were performed to understand the catalyst dependence of rate capability of the Li–O_2 batteries. Fig. 3 compares the SEM images of the MnO_2 and RuO_2/MnO_2 electrodes in the pristine and discharged states (1000 mAh g^{-1}). Compared with the pristine electrodes, both the MnO_2 and RuO_2/MnO_2 electrodes show minor morphology changes after discharged to 1000 mAh g^{-1} at 400 mA g^{-1}. Both the electrodes maintain a fluffy porous structure, indicating that Li_2O_2 can generally realize the conformal growth on MnO_2 sheets at this moderate current, agreeing with the rate capability results in Fig. 2a. At 800 mA g^{-1}, some particles form on MnO_2 although its sheet-like structure is still visible, which means that the catalytic activity of MnO_2 cannot fully support the high-rate ORR. For RuO_2/MnO_2, the particles are invisible and the porous structure is well preserved, agreeing well the results of rate performance in Fig. 2b. At higher current rates of 1600 and 3200 mA g^{-1}, particles and particles aggregations are evident on the surface of the MnO_2 electrode. In addition, the pores in the MnO_2 are filled by the particles, suggesting that the crystallization behavior of Li_2O_2 on MnO_2 is greatly affected by the current density. By contrast, for the RuO_2/MnO_2 electrode, the fluffy porous structure can still be retained at a high current density up to 3200 mA g^{-1}. This indicates that Li_2O_2 can realize conformal growth on RuO_2/MnO_2 at high current rates. Selected area electron diffraction (SAED) patterns and XPS verify the reversible formation/decomposition of Li_2O_2 (ESI, Fig. S3).

TEM observation was performed to further reveal the different crystallization habits of Li_2O_2 on MnO_2 and RuO_2/MnO_2. As shown in Fig. 4a, a thin, fluffy Li_2O_2 layer forms on the surface of RuO_2-decorated MnO_2 sheets, forming a sheet-on-sheet structure. On the bare MnO_2 sheets, large, thick Li_2O_2 particles appear, forming a particle-on-sheet structure (Fig. 4b). The sharp difference should be closely related to the presence of RuO_2, which may act as the catalytically active sites for the nucleation/crystallization of Li_2O_2 due possibly to the relatively high binding energy of noble metal Ru with oxygen.[62] The synergic catalytic effect of MnO_2 then directs the conformal growth of Li_2O_2 sheets on MnO_2 sheets, realizing the "wetting" of Li_2O_2 on MnO_2 sheets. Note that the addition of LiI shows little influence on the morphology of the discharged electrodes (ESI, Fig. S4). Fig. 4 shows the schematic illustration of the different crystallization habits of Li_2O_2 on the two electrodes at a high current density. The conformal growth of thin sheet-like Li_2O_2 is favorable since thin-layer structure allows its easy decomposition at low overpotentials.[9,10,27,28] The conformal growth also renders intimate contact of Li_2O_2 with RuO_2/MnO_2 which promotes a rapid oxidation decomposition of Li_2O_2 due to its superior OER catalytic activity. SEM images (ESI, Fig. S5) show that Li_2O_2 can be completely decomposed on the RuO_2/MnO_2 electrode after charged to 1000 mAh g^{-1}. The decomposition of Li_2O_2 becomes easier with the co-catalytic effect of LiI through the reaction $I_2 + Li_2O_2 \rightarrow 2Li^+ + 2I^- + O_2$, where I_2 was generated from I^- during the charge process.[60] In contrast, on the MnO_2 electrode, Li_2O_2 particles are still visible after the recharge process. Even in the presence of LiI, the pores of MnO_2 are still clogged although the Li_2O_2 particles on the surface have been removed. These results suggest that RuO_2 does play a critical role in catalyzing both ORR and OER, and that the synergic effect of MnO_2 and RuO_2 is important to realize the excellent rate capability of the Li–O_2 batteries.

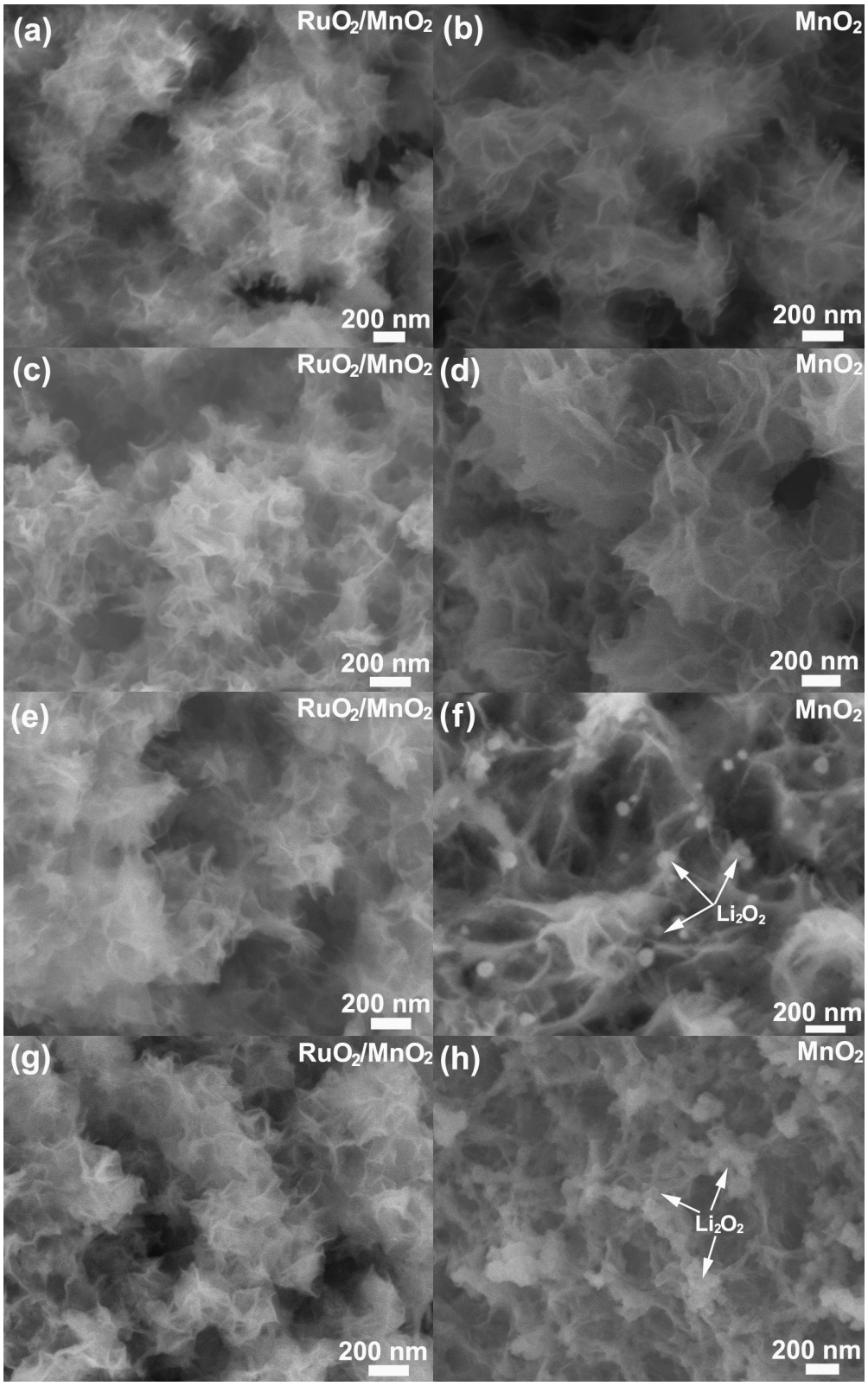

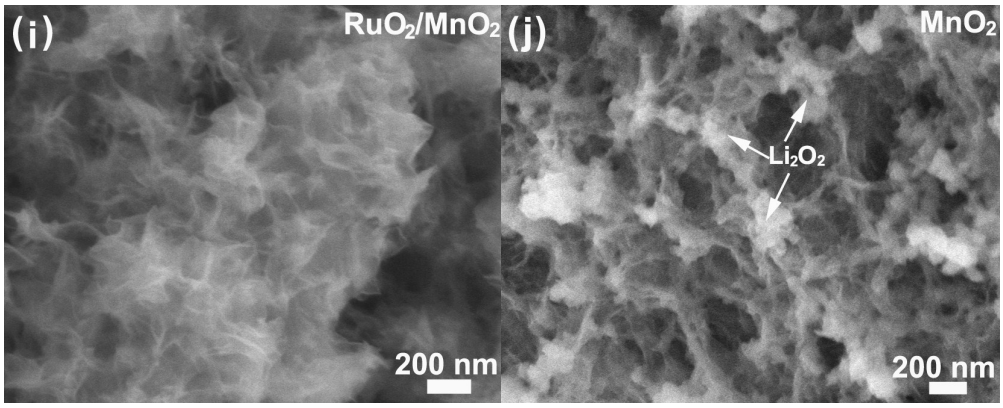

Fig. 3 SEM images of RuO_2/MnO_2 and MnO_2 electrodes at pristine states (a,b) and after discharged to 1000 mAh g^{-1} at (c,d) 400 mA g^{-1}, (e,f) 800 mA g^{-1}, (g,h) 1600 mA g^{-1} and (i,j) 3200 mA g^{-1}.

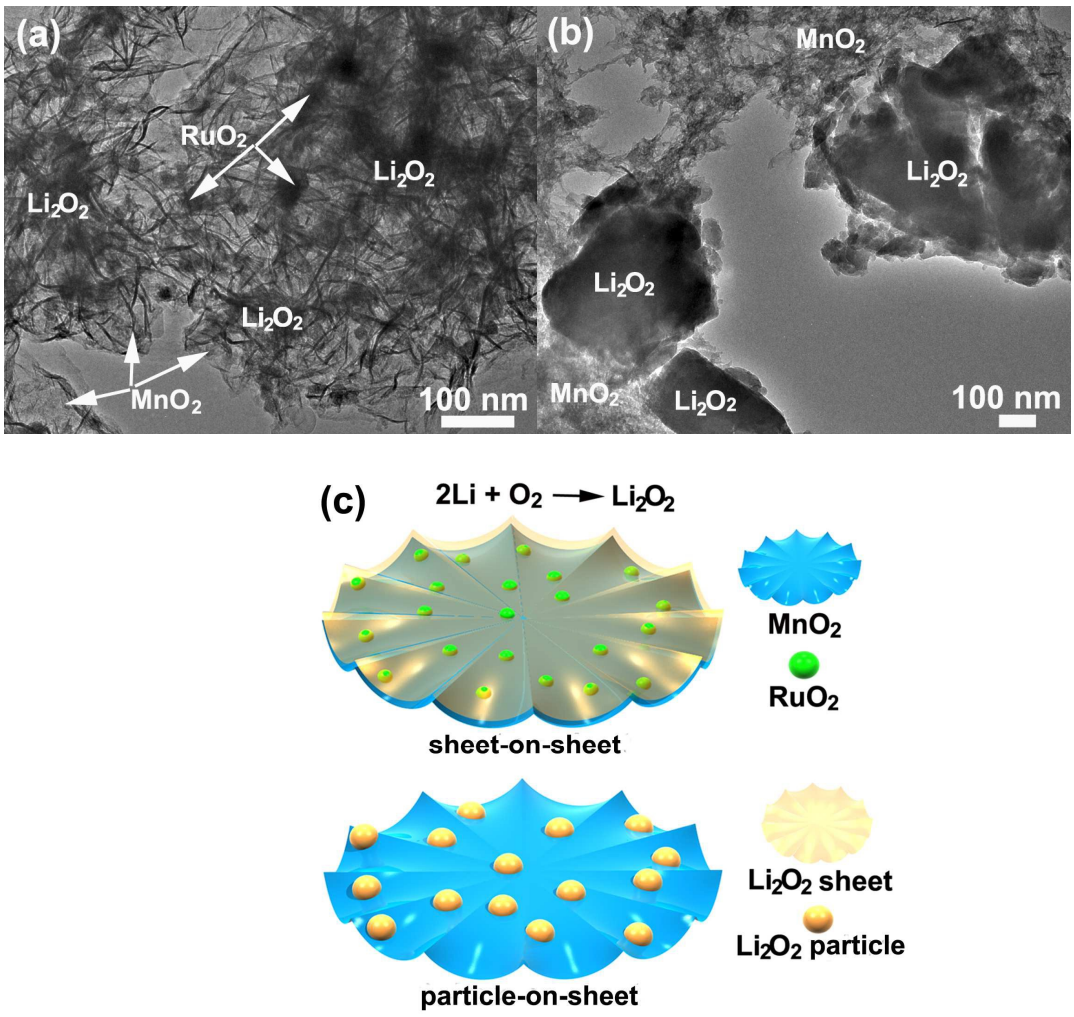

Fig. 4 TEM images of the (a) RuO_2/MnO_2 and (b) MnO_2 electrodes discharged to 1000 mAh g^{-1} at 3200 mA g^{-1}, and (c) formation mechanism of Li_2O_2 thin sheets or large particles on MnO_2 sheets with or without RuO_2 at high current density.

As discussed above, catalyst exerts great influence on the ORR especially at high current density. However, the intrinsic OER catalytic activity of the individual catalyst is unclear yet since besides catalyst, the morphology of the discharge product also affects the charge characteristics of the batteries. Therefore, the batteries were first discharged at a low current density of 200 mA g^{-1} to ensure similar morphology of Li_2O_2. At this low current density, the discharge curves are almost overlapped with a high potential plateau (~2.8 V), suggesting that MnO_2 itself can well support the ORR at low current rate (Fig. 5a). The charge behaviors, however, exhibit obvious catalyst dependence as seen in the figure. The OER catalytic activity is in the order of RuO_2/MnO_2+LiI > MnO_2+LiI > RuO_2/MnO_2 > MnO_2, roughly similar to the order in Fig. 2. With the synergic catalysis of RuO_2, MnO_2 and LiI, the Li–O_2 battery displays a rather low polarization with a mid-capacity overpotential of only 0.5 V. Besides rate capability, high-rate cycling stability is another important factor in determining the practical applications of Li–O_2 batteries. Before the capacity-limited cycling tests, the batteries were first fully discharged under 3200 mA g^{-1} to check the full capacities they can deliver at a high current density. It can be seen in Fig. 5b that Li–O_2 batteries with RuO_2/MnO_2+LiI, MnO_2+LiI, RuO_2/MnO_2 and MnO_2 catalysts deliver capacities of 1063, 1068, 1396, 1523 mAh g^{-1}, respectively. The battery with RuO_2 catalyst yields a higher capacity than that without RuO_2, due probably to the fact that the conformal growth of thin-layer Li_2O_2 on RuO_2-decorated MnO_2 sheets has deferred the deactivation of the electrodes, allowing more Li_2O_2 to be deposited.

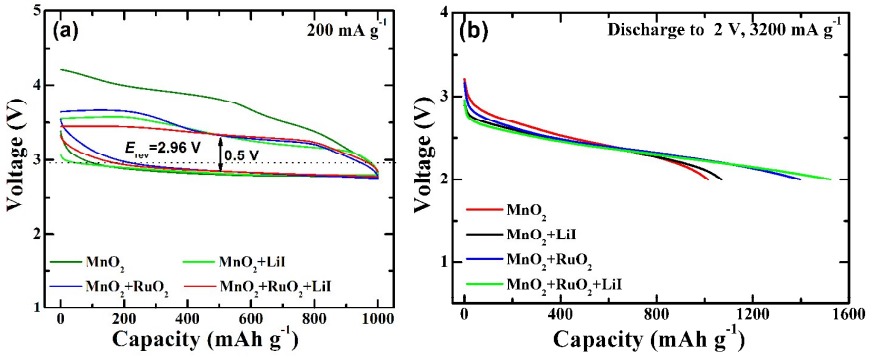

Fig. 5 The first voltage profiles of the Li–O_2 batteries with different catalysts tested (a) at 200 mA g^{-1} to 1000 mAh g^{-1} and (b) at 3200 mA g^{-1} discharged to 2 V.

The durability of the catalytic activity of the catalysts for ORR and OER at high rates was evaluated by cycling the Li–O_2 batteries at a high current rate. Fig. 6 shows the cycling performance of the Li–O_2 batteries with various catalysts at 3200 mA g^{-1} with the capacity limited at 1000 mAh g^{-1}. As seen in Fig. 6a, the Li–O_2 battery with MnO_2 catalyst can only sustain 30 cycles with high polarization (charge potential >4.3 V, discharge potential ~2.0 V). The poor cycling performance is attributed to the electrolyte decomposition at high potentials in the presence of Li_2O_2 (or LiO_2) and the accumulation of the byproducts, for instance $LiRCO_3$.[15,63] By adding soluble LiI catalyst, the cycling performance of MnO_2-catalyzed battery is much improved (Fig. 6b). After 170 cycles, a capacity of 989 mAh g^{-1} can be maintained, where the charge cutoff potential is below 4.2 V. The enhancement in cycling performance is due to the low oxidization potential of Li_2O_2 promoted by LiI (ESI, Fig. S5). The low oxidization potential of Li_2O_2, in turn, reduces decomposition of electrolyte. Compared with the MnO_2-catalyzed battery, the RuO_2/MnO_2-catalyzed battery also shows improved cycling performance (Fig. 6c). The improvement in battery performance can be ascribed to high catalytic ability of RuO_2 and the easy decomposition of thin-layer Li_2O_2. With the co-catalysis of RuO_2/MnO_2 and LiI, the cycling performance of the battery can be further improved (Fig. 6d). The stable cycling of the battery can last 170 times with a low charge cutoff potential (~4.0 V). After that, the performance degradation of the battery is probably due to the gradually weakened catalytic activity of the catalyst and/or the accumulation of inert byproducts that deactivate the electrode. As seen in Fig. S6, bare graphene on Ni shows rather low capacity and poor cycling performance, and can only be considered as the conductive substrate for RuO_2/MnO_2. For comparison, the catalytic activity of RuO_2 on grapheme (RuO_2/G) was also investigated. The RuO_2/G-catalyzed Li–O_2 battery can sustain a stable cycling of only 30 times with high overpotentials even at a low current density of 200 mA g^{-1} (ESI, Fig. S7a). SEM image in Fig. S7c shows that large Li_2O_2 particles form on the RuO_2/G electrode, indicating that the RuO_2 on graphene cannot induce the controlled growth of Li_2O_2 into thin-sheet form, in contrast to the case on MnO_2 sheets. The results suggest that both component and structure

should be taken into consideration to design highly efficient catalytic electrodes.

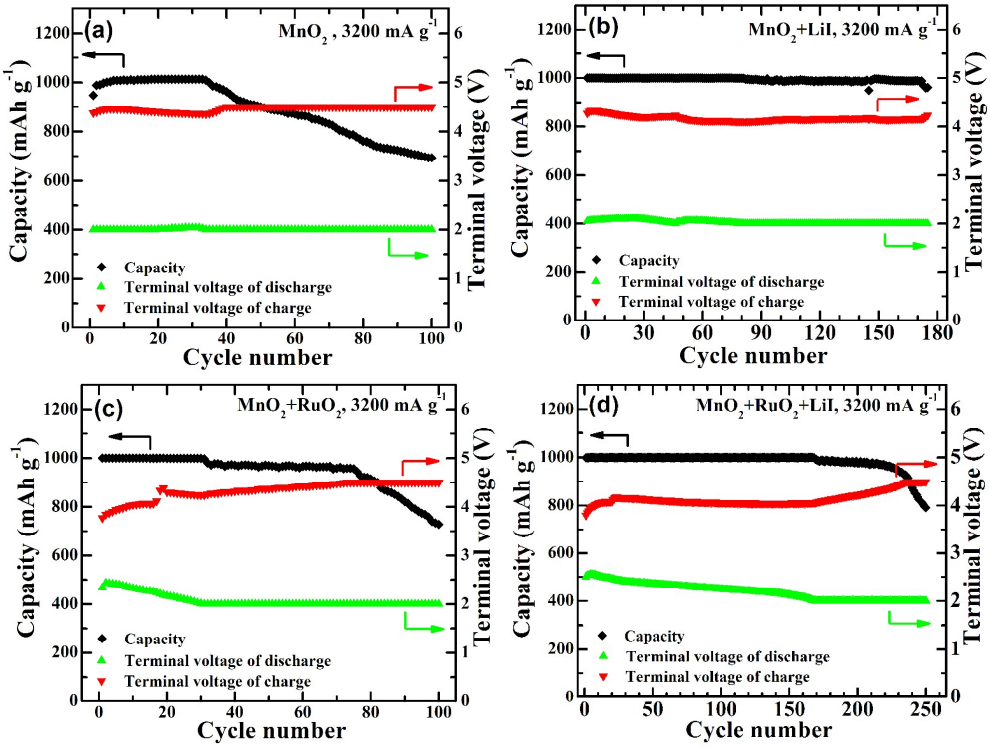

Fig. 6 Capacity and terminal voltage as a function of cycle number of the Li–O_2 batteries with different catalysts.

The cycling performance of the Li–O_2 battery with RuO_2/MnO_2+LiI catalyst was also evaluated at 800 mA g^{-1} with the capacity limited at 1000 mAh g^{-1} (Fig. 7a,b). At this current density, the battery shows a low overpotential in the initial cycles (Fig. 7a) and keeps a stable cycling of 180 times (Fig. 7b). As expected, the battery shows an obviously lower polarization compared with that operated at 3200 mA g^{-1}. After 180 cycles, the charge cutoff potential is still below 3.8 V, indicative of superior catalytic ability of RuO_2/MnO_2+LiI for Li_2O_2 oxidization. The battery was also cycled at a lower limited capacity of 500 mAh g^{-1} under 3200 mA g^{-1} (Fig. 7c,d). In this case, the battery can keep a stable cycling up to 800 times with a low charge cutoff potential (<3.8 V). After 1000 cycles, a capacity of 492 mAh g^{-1} is still retained with a relatively low charge cutoff potential (<4.0 V). The excellent high-rate cycling stability can be attributed to the optimized design of the catalytic cathode: (1) RuO_2/MnO_2 catalyzes the conformal growth of thin-layer Li_2O_2

on MnO_2 sheets; (2) thin-layer Li_2O_2 is easily oxidized by RuO_2/MnO_2+LiI at low potential with reduced electrolyte decomposition; (3) the side reactions related to binder and conductive carbon with Li_2O_2 (or LiO_2) can be totally excluded or largely minimized. Table 1 summaries the cycling performance of the Li–O_2 batteries with various catalysts, including MnO_2 and other metal oxides, RuO_2, and RuO_2-based mixed catalysts. The data in Table 1 represent the best ones reported most recently. The electrochemical performance of our RuO_2/MnO_2-catalyzed batteries is among the best ones when comparing the applied current density, terminal voltage, capacity and cycle life comprehensively. It should be stressed that the RuO_2/MnO_2 electrode is capable of controlling Li_2O_2 growth at high current density although its components (RuO_2, MnO_2) have been well studied as catalysts for Li–O_2 batteries. As a result, this work provides a unique design of catalytic cathode aiming at high-rate Li–O_2 batteries.

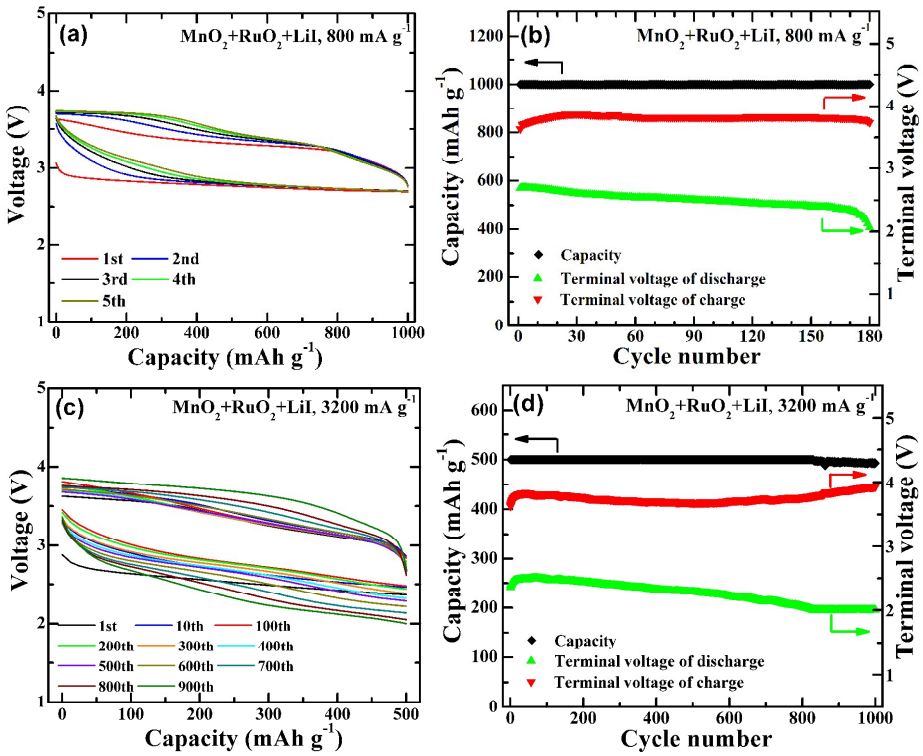

Fig. 7 Cycling performance of the Li–O_2 batteries with RuO_2/MnO_2+LiI catalyst tested (a) at 800 mA g^{-1} with a limited capacity of 1000 mAh g^{-1} and (b) at 3200 mA g^{-1} with a limited capacity of 500 mAh g^{-1}.

Table 1 Comparison of cycling performance of some metal oxides, RuO_2 and RuO_2-loaded oxides.

Sample/electrode preparation method	Current density	Terminal voltage range in the last cycle [V]	Charge/ discharge mode	Specific capacity	Cycle number	Reference
RuO_2/δ-MnO_2 directly grown on Ni	**3200 mA $g_{catalyst}^{-1}$ (~1.3 mA cm^{-2})**	**2.05 – 3.76 /2 – 4.07**	**Capacity limited**	**500 mAh $g_{catalyst}^{-1}$ /1000mAh $g_{catalyst}^{-1}$**	**800 /170**	**This work**
α-MnO_2/G paste coating	0.09 mA cm^{-2}	2.8 – 4.0	Capacity limited	580 mAh $g_{catalyst}^{-1}$	25	[35]
α-MnO_2/C paste coating	0.06 mA cm^{-2}	2.2 – 4.3	Capacity limited	500 mAh $g_{catalyst}^{-1}$	60	[36]
ε-MnO_2 directly grown on Ni	500 mA $g_{catalyst}^{-1}$	2.2 – 4.3	Capacity unlimited	>1000 mAh $g_{catalyst}^{-1}$	>120	[37]
δ-MnO_2/G directly grown on Ni	0.333 mA cm^{-2}	2.0 – 4.3	Capacity limited	492 mAh $g_{catalyst}^{-1}$	132	[38]
δ-MnO_2 aerogel paste coating	200 mA $g_{catalyst}^{-1}$	~2.3 – >4.5	Capacity limited	667 mAh $g_{catalyst}^{-1}$	25	[39]
ε-MnO_2 directly grown on Ni	500 mA $g_{catalyst}^{-1}$	2.2 – 4.0	Capacity limited	800 mAh $g_{catalyst}^{-1}$	190	[40]
Co_3O_4/G directly grown on Ni	0.1 mA cm^{-2}	>2.0 – ~4.5	Capacity limited	580 mAh $g_{catalyst}^{-1}$	62	[41]
Co-Mn-O nanocubes paste coating	0.16 mA cm^{-2}	> 2.0 – ~4.5	Capacity limited	500 mAh $g_{electrode}^{-1}$	100	[42]
mesoporous Co_3O_4 paste coating	0.1 mA cm^{-2}	>2.5 – ~4.2	Capacity limited	1000 mAh $g_{catalyst}^{-1}$	60	[43]
TiO_2 nanowires directly grown on carbon textiles	100 mA $g_{catalyst}^{-1}$	>2.0 in discharge	Capacity limited	500 mAh $g_{catalyst}^{-1}$	>356	[44]
macroporous $LaFeO_3$ paste coating	0.15 mA cm^{-2}	2.0 – ~4.75	Capacity limited	2000 mAh $g_{catalyst}^{-1}$	124	[45]
$LaNiO_3$ nanocubes paste coating	0.08 mA cm^{-2}	–	Capacity limited	500 mAh $g_{electrode}^{-1}$	75	[46]
porous $La_{0.5}Sr_{0.5}CoO_{2.91}$ paste coating	400 mA $g_{catalyst}^{-1}$	2.0 – ~4.75	Capacity limited	2000 mAh $g_{catalyst}^{-1}$	85	[47]
RuO_2/CNT paste coating	0.05 mA cm^{-2}	<2.5 – >4.0	Capacity limited	680 mAh $g_{catalyst}^{-1}$	20	[31]
RuO_2/G paste coating	500 mA $g_{catalyst}^{-1}$	~2.7 – ~3.9	Capacity limited	5000 mAh $g_{catalyst}^{-1}$	30	[49]
RuO_2/CNT paste coating	500 mA $g_{catalyst}^{-1}$	2.65 – 3.62	Capacity limited	300 mAh $g_{catalyst}^{-1}$	100	[50]
RuO_2/porous carbon paste coating	250 mA $g_{catalyst+carbon}^{-1}$	~2.5 – ~4.75	Capacity limited	1000 mAh $g_{catalyst+carbon}^{-1}$	300	[51]
RuO_2 hollow spheres paste coating	500 mA $g_{catalyst}^{-1}$	2.3 – 4.0	Capacity unlimited	~1000 mAh $g_{catalyst}^{-1}$	100	[52]
γ-MnO_2/RuO_2 paste coating	0.1 mA cm^{-2}	>2.0 in discharge	Capacity limited	1344 mAh $g_{catalyst}^{-1}$	50	[53]
TiO_2/RuO_2 directly grown on Ti	1770 mA $g_{catalyst}^{-1}$	~1.25 – ~3.5	Capacity limited	1000 mAh $g_{catalyst}^{-1}$	130	[54]
α-MnO_2/RuO_2 paste coating	0.1 mA cm^{-2}	>2.5 – 4.0	Capacity limited	300 mAh $g_{catalyst}^{-1}$	50	[55]

Note: G=graphene, CNT=carbon nanotube

XPS characterization was performed to clarify the excellent cycling stability of the Li–O_2 batteries catalyzed by RuO_2/MnO_2+LiI. Fig. 8a gives the C1s XPS of the electrodes cycled at different states. The broad peak at 283–286 eV can be assigned to C–C and C=C configurations in graphene.[64] After

repeated cycling, the peak keeps almost unchanged, indicating that it is stable in the battery system. Note that after 180 cycles, some peaks related to carboxylate, Li_2CO_3, and ethers become obvious but not significant, which is related mainly to electrolyte decomposition reactions.[15, 44] The formation of these byproducts can explain the performance degradation of the battery after long-term operation. However, the byproducts from the reactions between Li_2O_2 (or LiO_2) and carbon (graphene)[15–18] should be minor with our optimized electrode design. In addition, the catalyst-enabled low charge potentials in our case also reduce the electrolyte decomposition. It is expected that the cycling stability of the battery can be further improved by using stable electrolyte.

The intrinsic catalytic mechanism of RuO_2/MnO_2 during cycling was further investigated by XPS. It was found that the shape and position of Mn 2p peaks show minor changes upon discharge and charge and long-term cycling (Fig. 8b). This indicates that δ-MnO_2 is chemically/electrochemically stable against the attack of Li_2O_2 or LiO_2. Li–MnO_2/G battery tested in pure argon yields a small capacity even at a low current density (Fig. S8a), which indicates that only a small amount of lithium would be inserted into MnO_2 at high current density under O_2 atmosphere, agreeing with the XPS result. It is thus anticipated that a slight lithiation of MnO_2 should not exert obvious influence on the catalytic activity of MnO_2, although pre-lithiated MnO_2 has proved to show enhanced catalytic activity compared with the pristine one.[65] The position of Ru 3d peaks also show a minor change upon discharge and charge (Fig. 8c), indicating that the RuO_2 phase has been retained during charge and discharge. Li–RuO_2/G battery tested in pure argon also shows a small capacity even at a low current density (Fig. S8b), which suggests that the conversion reaction from RuO_2 to Ru is not obvious, in support of the XPS result. It is reasonable since the conversion reaction from RuO_2 to Ru occurs dominantly below 2.0 V.[66] These results suggest that RuO_2/MnO_2 itself exhibits intrinsically high catalytic activity.

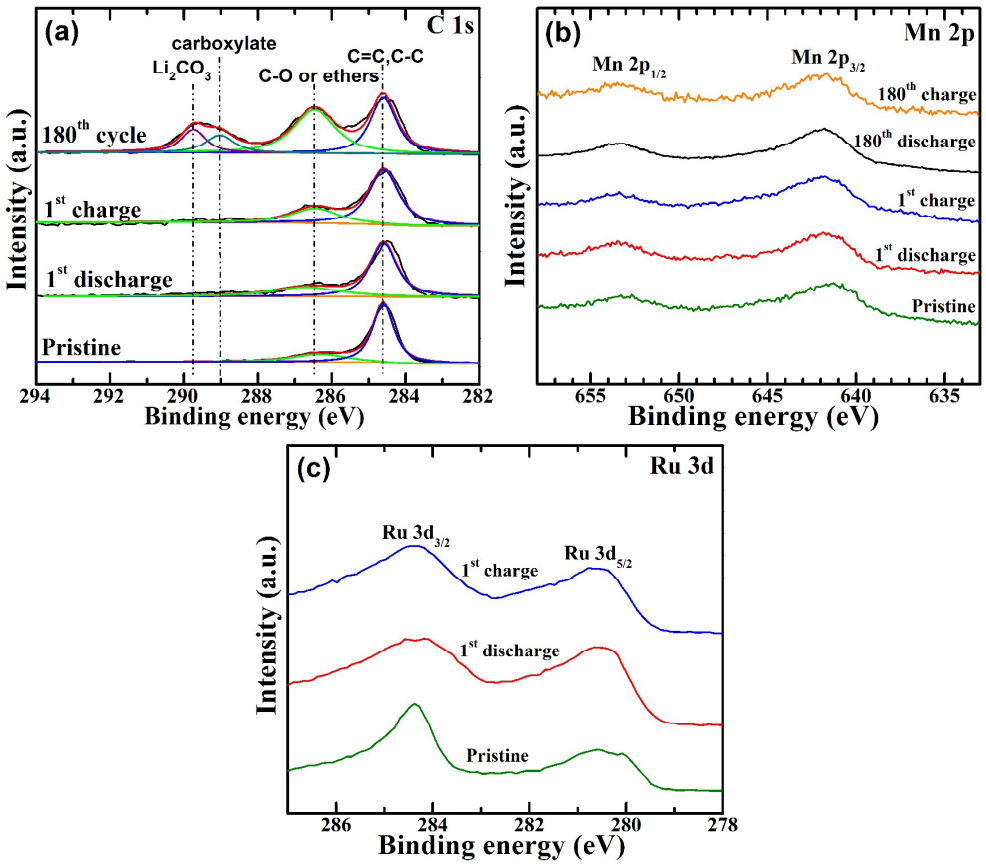

Fig. 8 (a) C1s, (b) Mn2p and (c) Ru3d XPS of the RuO_2/MnO_2 electrodes at different charge and discharge states.

Conclusions

In summary, we grew nanostructured RuO_2/MnO_2 catalyst directly onto graphene-coated nickel foam without using polymer binder. This electrode design totally avoids or largely excludes the side reactions between binder/carbon and Li_2O_2 (or LiO_2), allowing the revelation of the intrinsic catalytic performance of the catalysts. The RuO_2 nanocrystals on MnO_2 nanosheets show the ability to promote the conformal growth of thin-layered Li_2O_2 on MnO_2 at high current rates. The decomposition of thin-layer Li_2O_2 can be easily achieved by the excellent catalytic effect of RuO_2/MnO_2 and the promotion effect of LiI, leading to superior rate capability of the Li–O_2 batteries. At a current rate as high as 3200 mA g^{-1} (~1.3 mA cm^{-2}), the battery can demonstrate a low charge cutoff potential of 3.84 V and a high discharge cutoff potential of 2.54 V at a limited capacity of 1000 mAh g^{-1}. The Li–O_2 batteries also exhibit superior high-rate cycling stability,

sustaining a stable cycling of 170 times under 3200 mA g^{-1} at 1000 mAh g^{-1} with a relatively low charge cutoff potential (~4.0 V). A long cycle life over 800 times at 3200 mA g^{-1} can be achieved when the capacity is limited at 500 mAh g^{-1}. The superior high-rate cycling stability can be attributed to the controlled growth of Li_2O_2 at high rates catalyzed by RuO_2/MnO_2, the easy catalytic decomposition of Li_2O_2 by RuO_2/MnO_2+LiI at low potentials with reduced electrolyte oxidization, and minimized or excluded side reactions related to binder and carbon. The high catalytic activity of RuO_2/MnO_2 makes it a promising catalyst for high-rate Li–O_2 batteries.

Acknowledgements

This work was supported by the National Basic Research Program of China (2013CB934001), the National Natural Science Foundation of China (No. 51572238), Zhejiang Provincial Natural Science Foundation of China under Grant No. LY15E010004, the Fundamental Research Funds for the Central Universities (2014XZZX002–03), Key Science and Technology Innovation Team of Zhejiang Province under Grant Number 2010R50013, Program for Innovative Research Team in University of Ministry of Education of China (IRT13037), and Open Research Fund of Top Key Discipline of Chemistry in Zhejiang Provincial Colleges and Key Laboratory of the Ministry of Education for Advanced Catalysis Materials (Zhejiang Normal University). We acknowledge the access to the microscope facilities provided by the Center for Electron Microscopy of Zhejiang University.

Notes and references

1 F. T. Wagner, B. Lakshmanan and M. F. Mathias, *J. Phys. Chem. Lett.*, 2010, **1**, 2204–2219.

2 M. M. Thackeray, C. Wolverton and E. D. Isaacs, *Energy Environ. Sci.*, 2012**, 5**, 7854–7863.

3 P. G. Bruce, S. A. Freunberger, L. J. Hardwick and J. M. Tarascon, *Nat. Mater.*, 2012, **11**, 19–29.

4 K. M. Abraham and Z. Jiang, *J. Electrochem. Soc.*, 1996, **143**, 1–5.

5 T. Ogasawara, A. Débart, M. Holzapfel, P. Novák and P. G. Bruce, *J. Am. Chem. Soc.*, 2006, **128**, 1390–1393.

6 G. Girishkumar, B. McCloskey, A. C. Luntz, S. Swanson and W. Wilcke, *J. Phys. Chem. Lett.*, 2010, **1**, 2193–2203.

7 V. Viswanathan, K. S. Thygesen, J. S. Hummelshøj, J. K. Nørskov, G. Girishkumar, B. D. McCloskey and A. C. Luntz, *J. Chem. Phys.*, 2011, **135**, 214704.

8 O. Gerbig, R. Merkle and J. Maier, *Adv. Mater.*, 2013, **25**, 3129–3133.

9 M. D. Radina and D. J. Siegel, *Energy Environ. Sci.*, 2013, **6**, 2370–2379.

10 A. Dunst, V. Epp, I. Hanzu, S. A. Freunbergera and M. Wilkening, *Energy Environ. Sci.*, 2014, **7**, 2739–2752.

11 K. R. Ryan, L. Trahey, B. J. Ingram and A. K. Burrell, *J. Phys. Chem. C*, 2012, **116**, 19724−19728.

12 R. Younesi, M. Hahlin, M. Treskow, J. Scheers, P. Johansson and K.Edström, *J. Phys. Chem. C*, 2012, **116**, 18597−18604.

13 R. Younesi, M. Hahlin, F. Björefors, P. Johansson and K. Edström, *Chem. Mater.*, 2013, **6**, 77–84.

14 R. Black, S. H. Oh, J. H. Lee, T. Yim, B. Adams and L. F. Nazar, *J. Am. Chem. Soc.*, 2012, **134**, 2902−2905.

15 B. D. McCloskey, A. Speidel, R. Scheffler, D. C. Miller, V. Viswanathan, J. S. Hummelshøj, J. K. Nørskov and A. C. Luntz, *J. Phys. Chem. Lett.*, 2012, **3**, 997−1001

16 M. M. Ottakam Thotiyl, S. A. Freunberger, Z. Q. Peng and P. G. Bruce, *J. Am. Chem. Soc.*, 2013, **135**, 494−500.

17 B. M. Gallant, R. R. Mitchell, D. G. Kwabi, J. G. Zhou, L. Zuin, C. V. Thompson and Y. Shao Horn, *J. Phys. Chem. C*, 2012, **116**, 20800−20805.

18 D. M. Itkis, D. A. Semenenko, E. Y. Kataev, A. I. Belova, V. S. Neudachina, A. P. Sirotina, M. Hävecker, D. Teschner, A. Knop Gericke, P. Dudin, A. Barinov, E. A. Goodilin, Y. Shao Horn and L. V. Yashina, *Nano Lett.*, 2013, **13**, 4697−4701.

19 Y. Y. Shao, S. Park, J. Xiao, J. G. Zhang, Y. Wang and J. Liu, *ACS Catal.*, 2012, **2**, 844−857.

20 Y. C. Lu, B. M. Gallant, D. G. Kwabi, J. R. Harding, R. R. Mitchell, M. S. Whittingham and Y. Shao Horn, *Energy Environ. Sci.*, 2013, **6**, 750–768.

21 F. J. Li, T. Zhang and H. S. Zhou, *Energy Environ. Sci.*, 2013, **6**, 1125–1141.

22 M. Balaish, A. Kraytsberg and Y. Ein Eli, *Phys. Chem. Chem. Phys.*, 2014, **16**, 2801–2822.

23 Z. L. Wang, D. Xu, J. J. Xu and X. B. Zhang, *Chem. Soc. Rev.*, 2014, **43**, 7746–7786.

24 A. C. Luntz and B. D. McCloskey, *Chem. Rev.*, 2014, **114**, 11721–11750.

25 D. G. Kwabi, N. Ortiz Vitoriano, S. A. Freunberger, Y. Chen, N. Imanishi, P. G. Bruce and Y. Shao Horn, *MRS Bull.*, 2014, **39**, 443–452.

26 J. Lu, L. Li, J. B. Park, Y. K. Sun, F. Wu and K. Amine, *Chem. Rev.*, 2014, **114**, 5611−5640.

27 M. D. Radin, J. F. Rodriguez, F. Tian and D. J. Siegel, *J. Am. Chem. Soc.*, 2012, **134**, 1093−1103.

28 Y. X. Hu, X. P. Han, F. Y. Cheng, Q. Zhao, Z. Hu and J. Chen, *Nanoscale*, 2014, **6**, 177–180.

29 J. J. Xu, Z. L. Wang, D. Xu, L. L. Zhang and X. B. Zhang, *Nat. Commun.*, 2013, **4**, 2438.

30 H. D. Lim, H. Song, H. Gwon, K. Y. Park, J. Kim, Y. Bae, H. Kim, S. K. Jung, T. Kim, Y. H. Kim, X. Lepro, R. Ovalle Robles, R. H. Baughman and K. Kang, *Energy Environ. Sci.*, 2013, **6**, 3570–3575.

31 E. Yilmaz, C. Yogi, K. Yamanaka, T. Ohta and H. R. Byon, *Nano Lett.*, 2013, **13**, 4679−4684.

32 X. Huang, H. Yu, H. T. Tan, J. X. Zhu, W. Y. Zhang, C. Y. Wang, J. Zhang, Y. X. Wang, Y. B. Lv, Z. Zeng, D. Y. Liu, J. Ding, Q. C. Zhang, M. Srinivasan, P. M. Ajayan, H. H. Hng and Q. Y. Yan, *Adv. Funct. Mater.*, 2014, **24**, 6516–6523.

33 R. R. Mitchell, B. M. Gallant, Y. Shao Horn and C. V. Thompson, *J. Phys. Chem. Lett.*, 2013, **4**, 1060−1064.

34 B. M. Gallant, D. G. Kwabi, R. R. Mitchell, J. G. Zhou, C. V. Thompson, Y. Shao Horn, *Energy Environ. Sci.*, 2013, **6**, 2518–2528.

35 Y. Cao, Z. K. Wei, J. He, J. Zang, Q. Zhang, M. S. Zheng and Q. F. Dong, *Energy Environ. Sci.*, 2012, **5**, 9765–9768.

36 Y. Qin, J. Lu, P. Du, Z. H. Chen, Y. Ren, T. P. Wu, J. T. Miller, J. G. Wen, D. J. Miller, Z. C. Zhang and K. Amine, *Energy Environ. Sci.*, 2013, **6**, 519–531.

37 X. F. Hu, X. P. Han, Y. X. Hu, F. Y. Cheng and J. Chen, *Nanoscale*, 2014, **6**, 3522–3525.

38 S. Y. Liu, Y. G. Zhu, J. Xie, Y. Huo, H. Y. Yang, T. J. Zhu, G. S. Cao, X. B. Zhao and S. C. Zhang, *Adv. Energy Mater.*, 2014, **4**, 1301960.

39 S. Chen, G. X. Liu, H. Yadegari, H. H. Wang and S. Z. Qiao, *J. Mater. Chem. A*, 2015, **3**, 2559–2563.

40 X. F. Hu, F. Y. Cheng, X. P. Han, T. R. Zhang and J. Chen, *Small*, 2015, **11**, 809–813.

41 J. K. Zhang, P. F. Li, Z. H. Wang, J. S. Qiao, D. Rooney, W. Sun and K. N. Sun, *J. Mater. Chem. A*, 2015, 3, 1504–1510.

42 J. Zhang, L. J. Wang, L. L. Xu, X. M. Ge, X. Zhao, M. Lai, Z. L. Liu and W. Chen, *Nanoscale*, 2015, **7**, 720–726.

43 F. Wang, Z. Y. Wen, C. Shen, K. Rui, X. W. Wu and C. H. Chen, *J. Mater. Chem. A*, 2015, **3**, 7600–7606.

44 Q. C. Liu, J. J. Xu, D. Xu and X. B. Zhang, *Nat. Commun.*, 2015, **6**, 7892.

45 J. J. Xu, Z. L. Wang, D. Xu, F. Z. Meng and X. B. Zhang, *Energy Environ. Sci.*, 2014, **7**, 2213–2219.

46 J. Zhang, Y. B. Zhao, X. Zhao, Z. L. Liu and W. Chen, *Sci. Rep.*, 2014, **4**, 6005.

47 P. F. Li, J. K. Zhang, Q. L. Yu, J. S. Qiao, Z. H. Wang, D. Rooney, W. Sun and K. N. Sun, *Electrochim. Acta*, 2015, **165**, 78–84.

48 F. F. Tu, J. Xie, S. C. Zhang, G. S. Cao, T. J. Zhu and X. B. Zhao, *J. Mater. Chem. A*, 2015, **3**, 5714–5721.

49 H. G. Jung, Y. S. Jeong, J. B. Park, Y. K. Sun, B. Scrosati and Y. J. Lee, *ACS Nano*, 2013, **7**, 3532–3539.

50 Z. L. Jian, P. Liu, F. J. Li, P. He, X. W. Guo, M. W. Chen and H. S. Zhou, *Angew. Chem. Int. Ed.*, 2014, **53**, 442–446.

51 Z. Y. Guo, D. D. Zhou, H. J. Liu, X. L. Dong, S. Y. Yuan, A. S. Yu, Y. G. Wang and Y. Y. Xia, *J. Power Sources*, 2015, **276**, 181−188.

52 F. J. Li, D. M. Tang, T. Zhang, K. M. Liao, P. He, D. Golberg, A. Yamada and H. S. Zhou, *Adv. Energy Mater.*, 2015, **5**, 1500294.

53 K. Guo, Y. Li, J. Yang, Z. Q. Zou, X. Z. Xue, X. M. Li and H. Yang, *J. Mater. Chem. A*, 2014, **2**, 1509–1514.

54 G. Y. Zhao, Y. N. Niu, L. Zhang and K. N. Sun, *J. Power Sources*, 2014, **270**, 386−390.

55 H. Jang, A. Zahoor, J. S. Jeon, P. Kim, Y. S. Lee and K. S. Nahm, *J. Electrochem. Soc.*, 2015, **162**, A300−A307.

56 G. Zhao, R. Mo, B. Wang, L. Zhang and K. N. Sun, *Chem. Mater.*, 2014, **26**, 2551−2556.

57 X. J. Lin, X. Lu, T. Huang, Z. L. Liu and A. S. Yu, *J. Power Sources*, 2013, **242**, 855−859.

58 N. Ding, S. W. Chien, T. S. Andy Hor, R. Lum, Y. Zong and Z. L. Liu, *J. Mater. Chem. A*, 2014, **2**, 12433–12441.

59 N. Ding, Y. W. Lum, S. F. Chen, S. W. Chien, T. S. Andy Hor, Z. L. Liu and Y. Zong, *J. Mater. Chem. A*, 2015, **3**, 1853–1857.

60 H. D. Lim, H. Song, J. Kim, H. Gwon, Y. Bae, K. Y. Park, J. Hong, H. Kim, T. Kim, Y. H. Kim, X. Lepro, R. Ovalle Robles, R. H. Baughman and K. Kang, *Angew. Chem. Int. Ed.*, 2014, **53**, 3926–3931.

61 N. N. Feng, P. He and H. S. Zhou, *ChemSusChem*, 2015, **8**, 600–602.

62 Y. C. Lu, H. A. Gasteiger and Y.Shao Horn, *J. Am. Chem. Soc.*, 2011, **133**, 19048–19051.

63 B. D. McCloskey, D. S. Bethune, R. M. Shelby, G. Girishkumar and A. C. Luntz, *J. Phys. Chem. Lett.*, 2011, **2**, 1161–1166.

64 H. J. Shin, K. K. Kim, A. Benayad, S. M. Yoon, H. K. Park, I. S. Jung, M. H. Jin, H. K. Jeong, J. M. Kim, J. Y. Choi and Y. H. Lee, *Adv. Funct. Mater.*, 2009, **19**, 1987–1992.

65 Y. X. Hu, T. R. Zhang, F. Y. Cheng, Q. Zhao, X. P. Han and J. Chen, *Angew. Chem. Int. Ed.*, 2015, **54**, 4338–4343.

66. Y. Kim, S. Muhammad, H. Kim, Y. H. Cho, H. Kim, J. M. Kim and W. S. Yoon, *ChemSusChem*, 2015, **8**, 2378–2384.

Table of contents entry

RuO_2/MnO_2 catalyzed $Li–O_2$ batteries show excellent high-rate performance due to nano-RuO_2 enabled fast wetting of Li_2O_2 on MnO_2 nanosheets.